

INVESTIGATING THE MAGNETIC IMPRINTS OF MAJOR SOLAR ERUPTIONS WITH *SDO*/HMI HIGH-CADENCE VECTOR MAGNETOGRAMS

XUDONG SUN (孙旭东)¹, J. TODD HOEKSEMA¹, YANG LIU (刘扬)¹, MARIA KAZACHENKO², AND RUIZHU CHEN (陈瑞竹)^{1,3}

¹W. W. Hansen Experimental Physics Laboratory, Stanford University, Stanford, CA 94305, USA; xudong@sun.stanford.edu

²Space Sciences Laboratory, University of California, Berkeley, CA 94720-7450, USA

³Department of Physics, Stanford University, Stanford, CA 94305, USA

ABSTRACT

The solar active region photospheric magnetic field evolves rapidly during major eruptive events, suggesting appreciable feedback from the corona. Previous studies of these “magnetic imprints” are mostly based on line-of-sight only or lower-cadence vector observations; a temporally resolved depiction of the vector field evolution is hitherto lacking. Here, we introduce the high-cadence (90 s or 135 s) vector magnetogram dataset from the Helioseismic and Magnetic Imager (HMI), which is well suited for investigating the phenomenon. These observations allow quantitative characterization of the permanent, step-like changes that are most pronounced in the horizontal field component (B_h). A highly structured pattern emerges from analysis of an archetypical event, SOL2011-02-15T01:56, where B_h near the main polarity inversion line increases significantly during the earlier phase of the associated flare with a time scale of several minutes, while B_h in the periphery decreases at later times with smaller magnitudes and a slightly longer time scale. The dataset also allows effective identification of the “magnetic transient” artifact, where enhanced flare emission alters the Stokes profiles and the inferred magnetic field becomes unreliable. Our results provide insights on the momentum processes in solar eruptions. The dataset may also be useful to the study of sunquakes and data-driven modeling of the corona.

Keywords: Sun: flares — Sun: photosphere — Sun: magnetic fields

1. INTRODUCTION

Solar active regions (ARs) harbor strong magnetic fields that often carry significant electric currents. Processes such as flux emergence and shearing motion gradually bring excess magnetic energy into the low corona. During an eruption, the coronal magnetic field reorganizes rapidly, converting part of the magnetic energy into intense emission as flares, or propelling plasma into interplanetary space as coronal mass ejections (CMEs). There are two distinctive time scales in this “storage and release” picture (e.g. Schrijver 2009). In the plasma-dominated photosphere, the characteristic Alfvén speed (v_A) is low. Magnetic evolution leading to an eruption occurs over hours or days. In the lower corona, however, plasma β is low and v_A can reach a thousand kilometers per second. Flare emission and CME acceleration occur on a shorter time scale, on the order of 10 minutes.

Such a separation of time scales breaks down during major solar eruptions. There has been mounting evidence for the rapid evolution of the photospheric magnetic field associated with intense flares and fast CMEs (for a recent review, see Wang & Liu 2015). For example, permanent and step-wise changes have been observed in the line-of-sight (LoS) field component (B_l) for many large flares (e.g., Cameron & Sammis 1999; Kosovichev & Zharkova 2001; Sudol & Harvey 2005; Petrie & Sudol 2010). Changes up to several hundred

Gauss occur within mere minutes. In general, the LoS magnetic flux on the disk-ward side of the AR decreases, while the limb-ward flux increases, indicating a more horizontal magnetic configuration near the polarity inversion line (PIL; Wang et al. 2002; Wang & Liu 2010). The pattern is consistent with the observed darkening of the inner penumbrae and weakening of the outer penumbrae in δ -sunspots (Liu et al. 2005). The step-wise changes of B_l often start in the early phase of a flare, well before the soft X-ray (SXR) peak (Cliver et al. 2012; Johnstone et al. 2012; Burtseva et al. 2015).

This picture is consistent with vector field observations, which showed that the horizontal field component (B_h) and the shear angle near the main PIL increases after a flare (Wang 1992; Wang et al. 1994). In addition, B_h has been found to decrease in the peripheral areas of δ -sunspots (Wang et al. 2009). Since 2010, routine full-disk vector magnetograms from the Helioseismic and Magnetic Imager (HMI; Schou et al. 2012; Hoeksema et al. 2014) aboard the *Solar Dynamics Observatory* (*SDO*) have provided definitive evidence that the rapid, permanent photospheric field changes occur during most large flares (e.g., Wang et al. 2012a,b; Sun et al. 2012; Petrie 2012, 2013). A common scenario is that B_h increases significantly near the PIL, whereas the radial field component (B_r) varies less and without a clear pattern. The field becomes stronger and more inclined in the AR core.

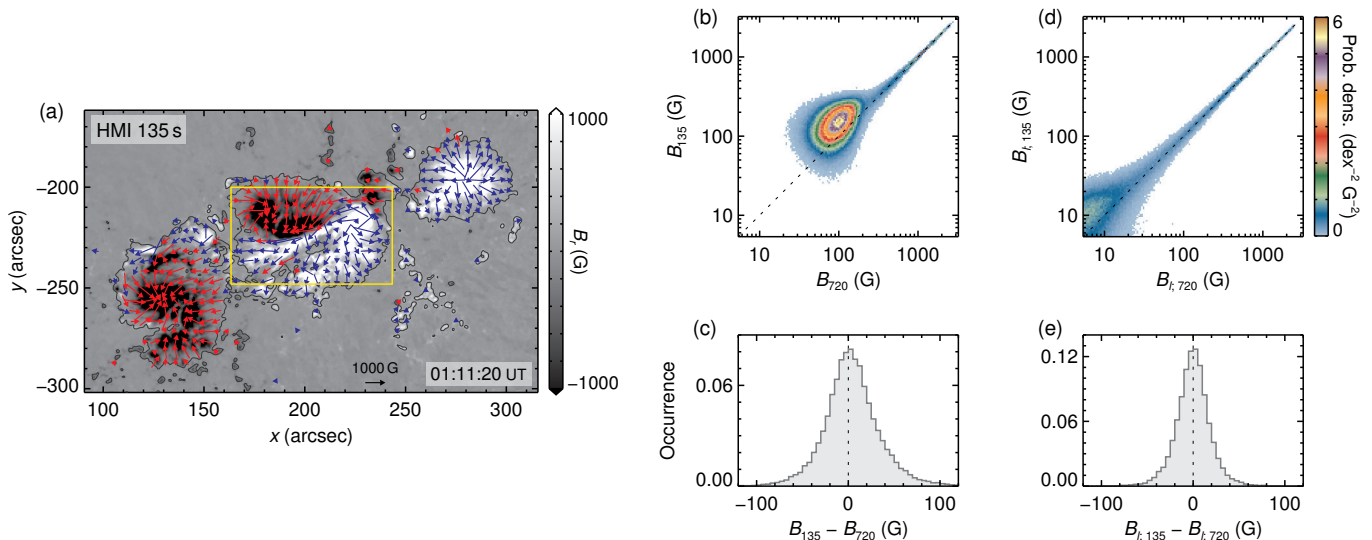


Figure 1. Comparison of 135 s and 720 s magnetograms for AR 11158 at 2011-02-15T01:11:20 UT. (a) Background image shows the 135 s radial field B_r . Arrows show horizontal field B_h . Contours show total field strength B at 300 G. The yellow box outlines the field of view for Figures 2–5. (b) Two-dimensional distribution of B for 135 s (B_{135}) and 720 s (B_{720}) data. Logarithm scale highlights the low field values. Dotted line has a slope of unity. (c) Distribution of $B_{135} - B_{720}$ for pixels with $B_{135}, B_{720} > 300$ G. (d) Similar to (b), but using only the absolute values of B_l when the two versions agree in sign. (e) Similar to (c), but for B_l .

The rapid appearance of these “magnetic imprints” suggests that they have a coronal origin, possibly as feedback from the eruption. In the “coronal implosion” conjecture (Hudson 2000), the non-erupting AR loops must contract to compensate for the loss of magnetic energy, which is consistent with the observed increase of field inclination. The impulsive coronal Lorentz force, which accelerates CME plasma to high speed, must act downward on the rest of the Sun due to momentum conservation (Hudson et al. 2008; Fisher et al. 2012). This back reaction has been evoked to explain sunquakes (Zharkov et al. 2011; Alvarado-Gómez et al. 2012) and sudden changes of sunspot rotation rate during flares (Wang et al. 2014; Liu et al. 2016a). Flares without a CME seem to exhibit weaker magnetic imprints than its eruptive counterpart (Sun et al. 2015).

Past observations have revealed much about the nature of magnetic imprints, but their LoS or lower-cadence nature leaves ambiguities in interpretation. For example, B_l generally contains a mixture of horizontal and radial field components, so the changes of B_h and B_r generally cannot be distinguished. Furthermore, the default HMI vector magnetograms have a cadence of 12 minutes and a wider, tapered temporal averaging window of ~ 22.5 minutes, so a large population of the rapid changes is not temporally resolved.

Another concern is the “magnetic transients”, where the field variations are impulsive and temporary, contrary to the more permanent magnetic imprints (e.g., Kosovichev & Zharkova 2001). The changes, which sometimes appear as a brief B_l sign reversal, seem to correlate with white-light or hard X-ray flare emission and are thought to be artifacts in-

duced by flare-altered line profiles (Qiu & Gary 2003; Abramenko & Baranovsky 2004). For the 12-minute-cadence HMI vector data processing, potentially anomalous line profiles may be averaged with normal ones, making diagnostics difficult.

To definitively characterize the rapid, vector field evolution, we have created a new high-cadence (90 s or 135 s) vector magnetogram dataset from HMI and use it to examine an archetypical event. Our intentions are twofold. Firstly, we provide a reference for the dataset by describing the key processing procedures and new features. Secondly, we demonstrate that the dataset is well suited for studying the magnetic imprints and transients in a quantitative and more temporally resolved manner. The new observations reveal a highly structured pattern of field evolution, which sheds light on the momentum processes in solar eruptions. We discuss the potential usage of the dataset for other studies.

2. DATA

HMI measures the Stokes parameters at six wavelengths in the photospheric Fe I 6173 Å absorption line. One of its two cameras is dedicated to the vector magnetic field. Under the original “Mod-C” observing scheme, vector magnetograms are inferred exclusively from this camera, and a full set of Stokes parameters (I, Q, U, V) requires 135 s to complete. Since April 2016, HMI has been operating under a new “Mod-L” observing scheme, which combines the polarization measurements from both cameras (Liu et al. 2016b; HMI Science Nugget #56). This results in reduced noise in the LoS component and a shorter, 90 s observing cycle. Under both

observing schemes, multiple sets of Stokes parameters are temporally averaged to suppress photon noise, leading to a routine vector magnetogram dataset with 720 s cadence.

We take advantage of the high-cadence Stokes measurement and create a new, full-disk vector magnetogram dataset with 135 s cadence ([hmi.B_135s](#)). The 90 s cadence version is under development. The dataset has the same format as the standard 720 s version (Hoeksema et al. 2014) and is processed with identical pipeline options except the following.

1. The filtergrams are interpolated linearly in time, and all contributing filtergrams are taken within 270 s (“quick-look” averaging scheme). This contrasts with the default, higher-order interpolation scheme and a wider temporal window that can produce artifacts when features are fast evolving (e.g., Martínez Oliveros et al. 2011).
2. A 50 G constant is added to the noise masks that are used as weak-field threshold in the 180° azimuth ambiguity resolution algorithm (Hoeksema et al. 2014) to account for the higher noise (see below).
3. Data will be processed for selective periods of significant activity and by request only. The first release of ~ 290 hr data covers about 30 events, most of which feature M- or X-class flares¹. The corresponding Stokes parameter dataset ([hmi.S_135s](#)) is also available.

The high-cadence data have higher noise due to shorter integration time and are more susceptible to contamination by p -mode oscillation. We illustrate this by comparing 135 s and 720 s data for AR 11158 at one instance (Figure 1(a)). The distribution of field strength B in the 135 s data (B_{135}) peaks at 129 G, while the 720 s data (B_{720}) peaks at 85 G (Figure 1(b)). These are typical values in the quiet Sun where the polarization degree is low, and the inferred B largely originates from photon noise. For B_l , the two frames are well correlated down to the deca-Gauss range (Figure 1(d)), suggesting that most noise resides in the transverse component.

We have carried out a similar comparison for 257 pairs of 135 s and 720 s full-disk B image over 6.4 days in February 2011. The median of B_{135} varies daily between about 155 and 175 G, presumably induced by *SDO*’s orbital velocity (Hoeksema et al. 2014). It varies in phase with the median of B_{720} , and is consistently ~ 50 G higher. We thus add 50 G to our noise mask for azimuth disambiguation.

In the example frame, the 135 s and 720 s data agree well in the strong-field regions. For pixels with $B > 300$ G, the differenced B (ΔB) and B_l (ΔB_l) have narrow distributions centered around 0 (Figures 1(c) and (e)). The half width half maximum (HWHM) is 25 and 17 G for ΔB and ΔB_l , respectively. For comparison, the median formal uncertainty of field strength σ_B derived from spectral line inversion is 35 and 28 G for the 135 s and 720 s data, respectively. Evolution also contributes to the difference.

¹For available time intervals and more details on the dataset, see <http://jsoc.stanford.edu/data/hmi/highcad>.

In this study, we focus on a 2 hr interval around an X-class flare on 2011 February 15, during which 54 frames of 135 s cadence data are available. We keep the images in the native Helioprojective-Cartesian coordinate, re-project the field vectors into a Heliocentric-spherical coordinate, and propagate the formal uncertainties (Sun 2013). We co-align the frames by cross-correlating continuum images obtained from inversion. The final dataset consists of cubes with a $250'' \times 170''$ field of view at a $0.''5$ pixel scale.

3. RESULTS

AR 11158 generated the first X-class flare of Cycle 24, SOL2011-02-15T01:56. An X2 flare and a fast CME originated from the central bipole in this quadrupolar AR, located at W20S10 (Schrijver et al. 2011; Sun et al. 2012). The flare ribbons exhibited an archetypical “double-J” morphology (Figure 2(a)), which then extended both along and away from the main PIL. The *GOES* SXR flare started, peaked, and ended at 01:44, 01:56, and 02:06, respectively. The *RHESSI* 25–50 keV hard X-ray (HXR) flux peaked at 01:54, two minutes before the SXR peak. The magnetic imprints and transients have been studied using routine HMI 45 s LoS and 720 s vector data (e.g., Kosovichev 2011; Wang et al. 2012a; Sun et al. 2012; Gosain 2012; Murya et al. 2012; Petrie 2013; Raja Bayanna et al. 2014).

We now re-examine the more rapid magnetic evolution using the 135 s vector dataset. We focus on the scalars B_h and B_r , and defer analysis of other variables such as azimuth and electric current to future studies. We utilize a new database for flare ribbons (Kazachenko et al. 2017) observed in 1600 Å by the Atmospheric Imaging Assembly (AIA). It corrects for spurious intensities associated with strong flare emission and provides easy access to the evolving ribbon morphology.

3.1. Example of Magnetic Imprint

The co-aligned, high-cadence data now allow us to perform meaningful temporal analysis on single pixels. Following Sudol & Harvey (2005), we use a step-like function to model the magnetic imprint in a time sequence of field component B_i ,

$$B_i(t) = a + bt + c \left\{ 1 + \frac{2}{\pi} \arctan[n(t - t_m)] \right\}, \quad (1)$$

where a , b , c , n , and t_m are free parameters. The term $a + bt$ accounts for linear evolution; $\Delta B_i = 2c$ measures the magnetic field change; t_m corresponds to the mid-time of change; $\tau = \pi n^{-1}$ characterizes the time scale of change; $t_s = t_m - \tau/2$ is the start time of change; and $dB_i/dt = \Delta B_i/\tau$ is the change rate. We employ a least-square Monte Carlo method for fitting, and quote the median and 1σ confidence interval when needed. To reduce the effect of noise, we consider only strong-field pixels, where $B > 300$ G. Additional details of modeling are presented in Section 3.3.

A base-difference map of B_h (Figure 2(a)) shows clear, structured patterns of field change. In particular, B_h increases

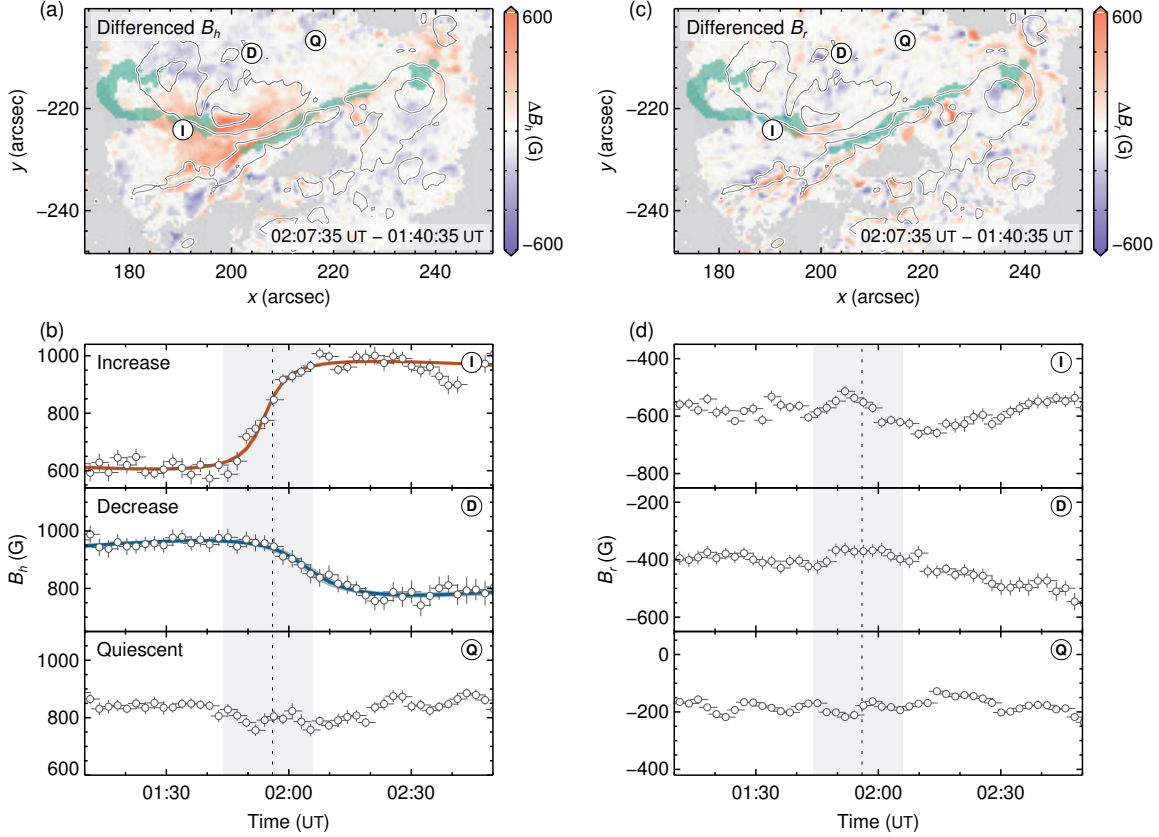


Figure 2. Rapid magnetic field evolution. (a) Base-differenced B_h map. Gray regions have $B < 300$ G. Green shades outline flare ribbons in AIA 1600 Å at 01:47:54. Contours are for B_r at ± 1000 and ± 2000 G. Symbols “I”, “D”, and “Q” mark the sample pixels, where B_h exhibits significant increase, decrease, or little change (quiescent), respectively. (b) Temporal evolution of B_h at sample pixels. Here and after, symbols show observations; horizontal error bars show the temporal averaging window of filtergrams; vertical error bars show formal uncertainty from spectral line inversion. Curves show a fitted step-like function. Vertical gray band indicates *GOES* flare time; vertical dotted line indicates SXR flare peak. (c)–(d) Similar to (a)–(b), but for B_r . (An [animation](#) of this figure is available.)

significantly near the main PIL between the flare ribbons, in agreement with previous findings (Wang et al. 2012a; Sun et al. 2012; Gosain 2012; Petrie 2013). An equally important aspect is the wide-spread, though somewhat weaker decrease of B_h further away from the PIL. A closer look at the temporal evolution of two representative pixels reveals clear, step-like changes that are well-resolved temporally (Figure 2(b)). The fit parameters ($\Delta B_h, t_m, \tau$) are $(468^{+35}_{-33}, 10.2^{+0.5}_{-0.5}, 13.4^{+2.5}_{-2.3})$ and $(-330^{+75}_{-103}, 20.5^{+1.6}_{-1.5}, 28.8^{+12.9}_{-10.5})$ for the two example pixels (in units of G, minute since flare start, and minute), respectively. The increase is stronger, occurs earlier, and evolves faster compared to the decrease. In contrast, the example quiescent profile is not well fitted by the step-like function.

To assess the significance of ΔB_h , we evaluate the secular evolution by differencing pairs of B_h maps both before or both after the flare. We choose a time lag of 11.25 minute (5 frames), which is close to the median of τ (see Section 3.3), i.e., typical magnetic imprint time scale. For 15 pre-flare and 19 post-flare pairs, the root mean square (rms) ΔB_h is 64 G,

and the rms formal uncertainty of ΔB_h is 68 G. We take the quadrature sum 93 G as the quiescent background. The changes at the two example pixels are thus at $5.0^{+0.4}_{-0.4}\sigma$ and $-3.5^{+0.8}_{-1.1}\sigma$, respectively.

In comparison, the variation of B_r is less pronounced and less structured (Figure 2(c)). There appear to be patchy changes along the flare ribbons of both increase and decrease. The quiescent background of ΔB_r is 76 G. Neither example pixels with step-like B_h change exhibit significant B_r change (Figure 2(d)).

3.2. Magnetic Transients

Magnetic transients have been reported for SOL2011-02-15T01:56 using HMI 45 s LoS data. They are associated with continuum enhancement and Doppler-velocity transients (Kosovichev 2011). The observed left- and right-circular-polarization profiles appear to be distorted (Raja Bayanna et al. 2014). HMI high-cadence Stokes data have been used to study magnetic transients too. For this event, transient changes occur in all Stokes parameters (Maurya et al. 2012).

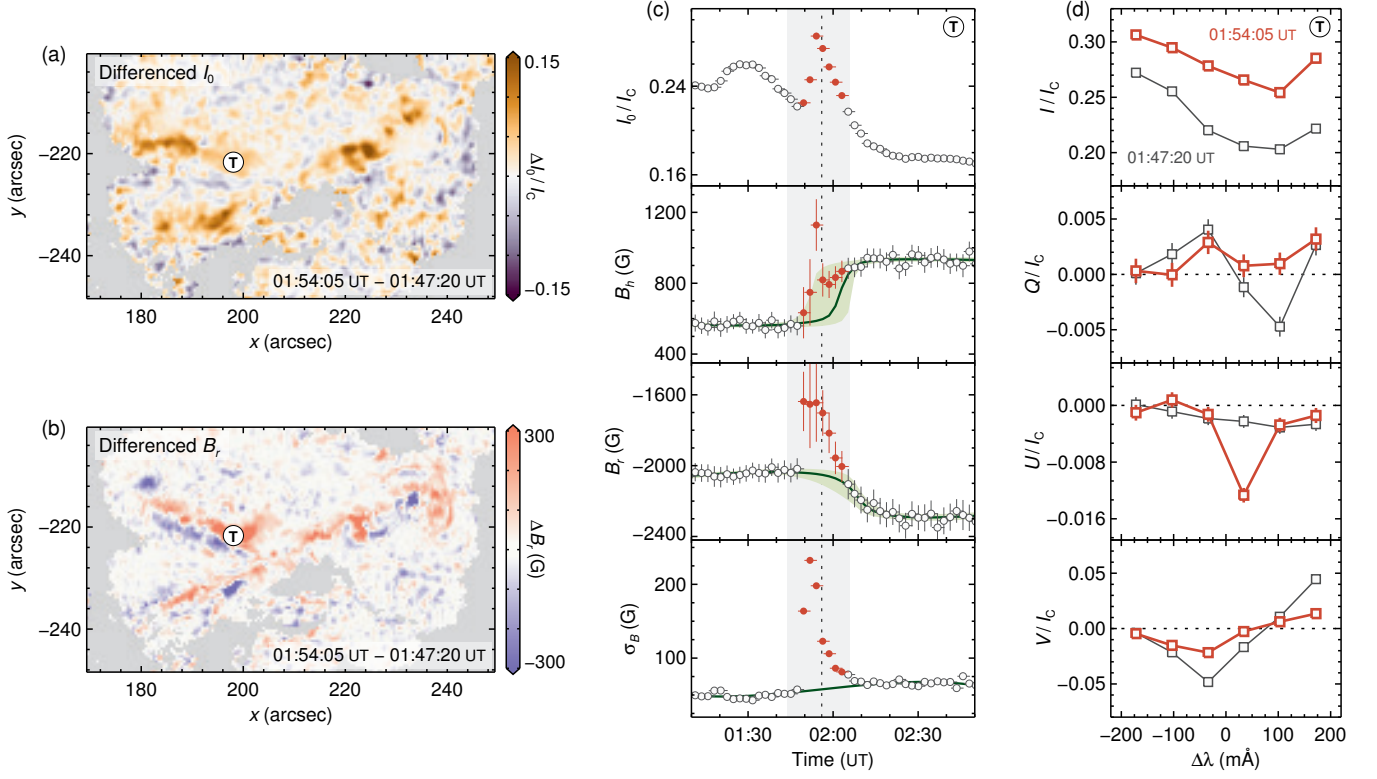


Figure 3. Flare-induced artifact as “magnetic transient”. (a) Differenced map of Stokes I_0 ($\Delta\lambda = +172$ mÅ offset from line center) near the flare peak, normalized to the quiet-Sun mean continuum I_c . Symbol “T” marks the sample pixel. (b) Differenced B_r map. (c) Temporal evolution of the sample pixel. Red symbols show the frames affected by flare emission. Green curves show the fitted step-like function for B_h and B_r and a fitted third-order polynomial for σ_B ; green bands show the 1σ fitting confidence interval. Larger fitting uncertainty during flare time is due to the fact that we exclude magnetic transients. (d) Stokes profiles of the sample pixel at two instances, near (red) and before (gray) the flare peak. Error bars are derived assuming Poisson statistics.

For an M7.9 flare SOL2012-03-13T17:41, transient changes in linear polarization appear to be consistent with genuine field evolution (Harker & Pevtsov 2013).

We search for transient signals first by inspecting running difference image sequences. In two elongated patches that resemble UV ribbons, Stokes I increases across the line profile by as much as 15% of the nearby mean quiet-Sun continuum value (I_c) during the flare impulsive phase (Figure 3(a)). Transient field changes appear in both B_h and B_r (Figure 3(b)), and are approximately co-spatial with Stokes I enhancement. We do not find obvious sign reversals in B_r .

Time profile of an example pixel (Figure 3(c)) exhibits a resolved transient change in both B_h and B_r during the flare, superposed on a step-like, permanent change. This suggests that the magnetic transient can occur in conjunction with the magnetic imprint. The increase starts early in the flare and reaches maximum slightly before the SXR peak. We find that the formal uncertainty of inferred field strength σ_B increases significantly during this period, nearly tripling the background. The Stokes profiles deviate from the pre-flare conditions (Figure 3(d)); polarization generally becomes weaker except for U near the line core. These observations

suggest that the Stokes profiles are distorted by flare emission and are not adequately modeled under the default settings of the spectral line inversion algorithm (Centeno et al. 2014). The inferred magnetic fields become less reliable.

To identify and characterize the magnetic transients, we apply the following four criteria with respective empirical identification schemes (Figures 3(c) and 4(a)).

1. The observation is made during the *GOES* flare time.
2. The pixel resides in the flare ribbons. The UV ribbons at each instant are expected to be much more extended than the white-light sources, and thus should safely encompass the impacted photospheric region. Our new AIA 1600 Å flare ribbon database provides co-aligned masks of ribbon locations at a 24 s cadence (Kazachenko et al. 2017), which we further dilate by ~ 3 Mm (8 pixels). For each HMI measurement time t , we create a “ribbon mask” that includes all pixels in the AIA masks within $t \pm 2$ minute.
3. The formal uncertainty of field strength, σ_B significantly exceeds the non-flaring background in a single-pixel time sequence. We mask out the time steps during the flare and fit a third-order polynomial to the rest, assuming there is

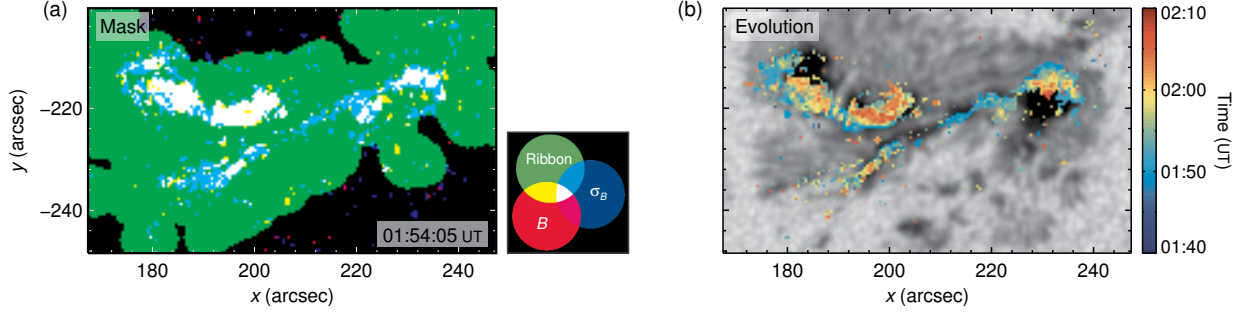


Figure 4. Identification and evolution of magnetic transients. (a) Masks for the 01:54:05 UT frame. AIA 1600 Å instantaneous flare ribbon mask is shown in green; mask for transient values in B_r or B_h time sequence is shown in red; mask for transient values in σ_B is shown in blue. Pixels where all three masks overlap are colored white and used as our final mask. (b) Evolution of the transient mask color-coded by time, overplotted on a pre-eruption I_0 map. (An [animation](#) of this figure is available.)

no sudden change in measurement quality during quiescent times. We mark those flare-time measurements that exceed the fit by more than three times the rms residual. For a single time step, all marked locations constitute a “ σ_B mask”.

4. The measured magnetic field B_h or B_r is an outlier in a single-pixel time sequence. We mask out all measurements of suspect quality identified in the previous step, and fit the rest with both a step-like function and a third-order polynomial. Using the better of the two models (smaller reduced chi-square χ_r^2), we mark those flare-time measurements that deviate from the fit by more than three times the rms residual, and create a “ B mask” for each time step.

The σ_B mask (blue in Figure 4(a)) and B mask (red) reside almost completely inside the ribbon mask (green), suggesting that the transient variations of the field measurement and its quality are indeed correlated with UV flare emission. The σ_B and B masks often overlap. However, there are cases where the quality of inversion is suspect but no transient signal is found in the inferred magnetic field (cyan). There are also cases where the field changes transiently but the quality of inversion remains similar (yellow), so there is no evidence against genuine field evolution. A detailed analysis of the Stokes parameters and the inversion result at these locations is necessary, but is out of the scope of this work.

Here, we narrowly define magnetic transients as measurements that satisfy all four criteria above (white in Figure 4(a)). By definition, they appear where the magnetic field cannot be reliably derived from flare-impacted Stokes observations. They cover about 6% of strong-field pixels in AR 11158. Our empirical scheme appears to work effectively at separating transients from magnetic imprints and secular evolution (Figure 3(c)). Interestingly, the location and evolution of the identified transients (Figure 4(b)) closely resemble that of the white-light sources in *Hinode* continuum observations (Kerr & Fletcher 2014), even though we have not explicitly used HMI Stokes I or continuum in our scheme. This further suggests that the photospheric impact of flare emission is a necessary condition for magnetic transients.

Transients identified in HMI LoS observations are similar in nature, as the essential assumption of a Gaussian line profile may break down. Additional artifacts may also come from our observing scheme. For example, the slightly different observation times of the Stokes parameters at different wavelengths can cause an undesirable aliasing effect (Martínez Oliveros et al. 2014).

3.3. Statistics of Magnetic Imprints

We now study the statistical behavior of magnetic imprints. After excluding the identified transient measurements, we fit the time sequence at each pixel with both a step-like function (for magnetic imprints) and a third-order polynomial (for secular evolution). Only pixels that favor the magnetic imprint model, that is, having a smaller χ_r^2 for the step-like function fit, are included in our analysis. About 5% of pixels with the poorest fit ($\chi_r^2 \geq 5.5$) are discarded.

We further apply several empirical selection criteria. To ensure that the profile is temporally resolved, we include only pixels where the time scale is longer than the cadence ($\tau \geq 135$ s) and the mid-change time is no earlier than the first observation since flare start ($t_m \geq 1.08$ minute)¹. We additionally require that the change starts after the flare onset ($t_s \geq 0$), but not too long after ($t_m < 36$ minute and $\tau < 1$ hr). The rate of field change of the magnetic imprint should also exceed that of the linear evolution $|dB/dt| > |b|$ (see Equation 1).

For B_h , 15% (about 4200) strong-field pixels are finally selected (Figure 5). In particular, we compare two subregions (Box “I” and “D”), which contain about 250 well fitted pixels each. Our analysis indicates the following.

1. Magnetic imprints appear over the entire AR. Most imprinted pixels are located in the inner or the outer penumbra of the central sunspot pair. The former resides along the PIL between the flare ribbons; the latter brackets the ribbons.

¹In practice, fitting is performed within the following limits to ensure a physically meaningful imprint model: $1.08 \leq t_m \leq 37.08$ minute (from 01:45:05 to 02:21:05) and $2.25 \leq \tau \leq 63.62$ minute (from 1 to 9π time steps). Fits hitting any limit (e.g., $t_m = 1.08$ or $\tau = 2.25$) are excluded.

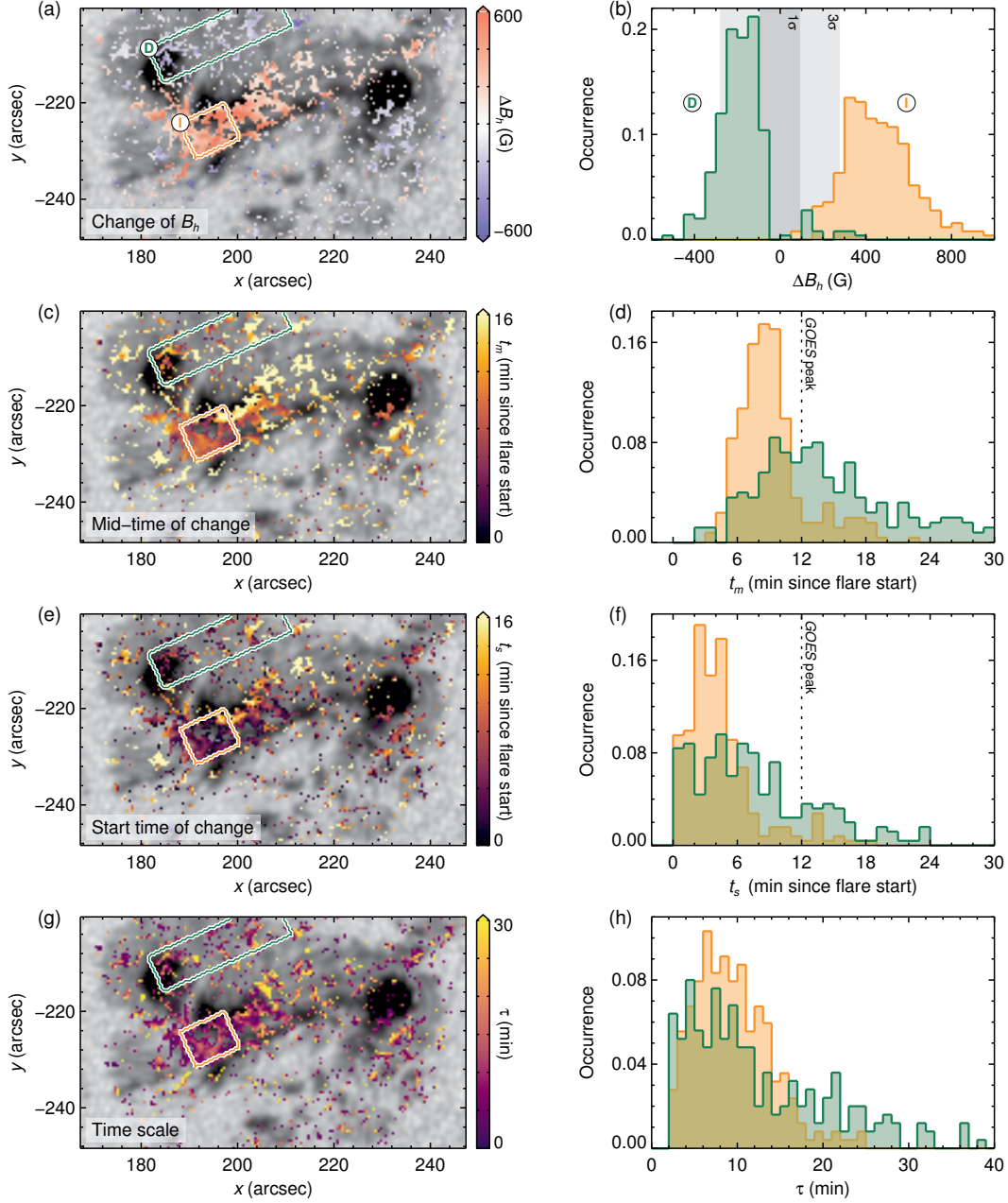


Figure 5. Characteristics of the field evolution derived from the step-like function fit after correcting for magnetic transients. (a) Horizontal field change ΔB_h , overlaid on a pre-eruption I_0 map. Only pixels with reasonable fits are included (see the text for details). The two subregions marked as “I” and “D” are selected for comparison. (b) Histogram of ΔB_h in subregions “I” and “D”. Darker and lighter gray bands indicate 1σ and 3σ quiescent background, respectively. (c)–(d) Similar to (a)–(b), but for the mid-time of change t_m . Vertical dotted lines in (d) indicates *GOES* SXR peak time. (e)–(f) Similar to (a)–(b), but for the start time of change t_s . (g)–(h) Similar to (a)–(b), but for the time scale of change τ .

2. The magnitude of change ΔB_h is almost exclusively positive in Box “I” and negative in Box “D” (Figures 5(a) and (b)). Box “I” has a median increase of 441 G (4.7σ , the quiescent background). Box “D” shows a weaker decrease with a median of -174 G (1.9σ). While ΔB_h may not be significant at individual pixels, the wide-spread, coherent pattern of change is striking. A two-sample Kolmogorov-

Smirnov (K-S) test¹ on ΔB_h in Box “D” confirms that the changes during the eruption are very different from quiescent evolution.

¹We compare the distribution of ΔB_h in a difference B_h map spanning the eruption (Figure 2(a)) with seven difference maps before the eruption. The K-S test median K is 0.510, and in all cases $p \ll 10^{-5}$. We thus reject the null hypothesis that ΔB_h of magnetic imprints and quiescent evolution are drawn from the same distribution.

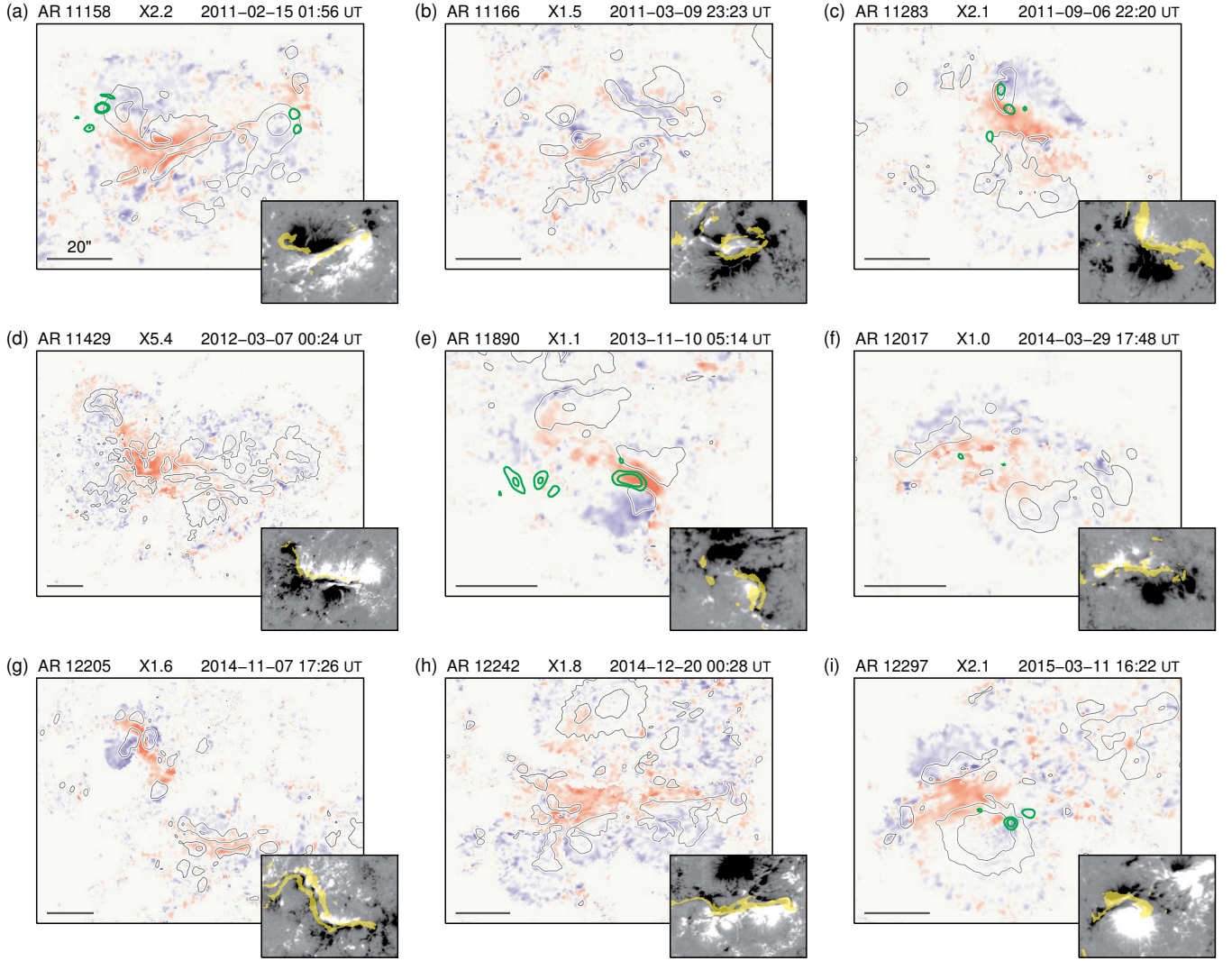


Figure 6. Overview of magnetic imprints in nine arbitrarily selected events with X-class flares from the first data release. Each panel shows base-differenced B_h map scaled between ± 600 G with B_r contours at ± 1000 and ± 2000 G, same as Figure 2(a). Insets show B_r maps scaled between ± 1000 G with 1600 Å flare ribbons observed early during the flare overlaid. In panels (a), (c), (e), (f), and (i), green contours show the 6 mHz egression power at 3σ and 6σ (quiet-Sun rms) around flare peak as possible sunquake sources (Chen & Zhao 2016). Scale bars are 20'' in all panels.

3. The increases in Box “I” occur early during the flare, with median t_m and t_s of 8.6 and 3.8 minutes (since flare start; Figures 5(c)–(f)), respectively. These are much earlier than the SXR peak at 12 minutes and the HXR peak at 10 minutes. The decreases in Box “D” occur slightly later. Parameters t_m and t_s have a wider distribution and median of 13.1 and 6.5 minute, respectively. Almost all pixels (99%) start changing during the flare ($t_s < 22$ minute).
4. The median time scale of change τ is 8.9 minute for Box “I” and 10.1 minute for Box “D” (Figures 5(g) and (h)). The decreases occur more slowly, as about 22% of pixels have $\tau > 20$ minute.

These results and our selection criteria deserve some discussion. Firstly, the magnetic imprints appear to be spatially

separated from the magnetic transients despite some overlap (see Figures 5(a) and 4(b)). About 40% of transient pixels are co-spatial with imprints, while only 9% of imprints are marked for transients. Secondly, our requirement that the field change must occur after the flare onset is purely empirical, which aims to establish some causal relations between the imprint and the flare. However, many excluded pixels (28% of the final selection) satisfy all other criteria but have $-5 \leq t_s < 0$ minute. Given the measurement uncertainties, it is possible that they are genuine magnetic imprints. It is also possible that magnetic evolution can indeed precede flare onset. Thirdly, a significant number of excluded pixels (89% of the final selection) have a small τ ; their step-like changes are not resolved at HMI’s cadence. This is compatible to B_l observations, where $\sim 50\%$ (Sudol & Harvey 2005) and $\sim 25\%$

(Petrie & Sudol 2010) of all events occur on a time scale of less than 2 minutes. Fourthly, the spatial distribution of t_m (Figure 5(c)) suggests that the B_h changes “propagate” across the AR from the main PIL, similar to the findings in Sudol & Harvey (2005) using B_l observations.

We apply the same procedures on B_r and find many pixels with clear step-wise changes significantly above the quiescent background (for a marked example, see Figure 3(c)). Nevertheless, the changes appear much less structured spatially and temporally. We do not attempt to make further conclusions.

4. DISCUSSION AND OUTLOOK

The new high-cadence vector dataset allows us to quantitatively depict a scenario where flare-associated magnetic imprints, mainly appearing as step-wise, persistent changes in B_h , occur over the entire AR with a spatially and temporally structured pattern. Along the main PIL, B_h increases rapidly during the early phase of the flare, whereas in the AR periphery B_h decreases more slowly and at later times. The field change is typically a few hundred Gauss, well above the quiescent background evolution, and stronger for the increase than decrease. The time scale of temporally resolved changes is about 10 minutes; a significant portion is still unresolved at HMI’s 135 s cadence.

We note that detailed temporal analysis has hitherto been limited to B_l . Depending on the AR’s location, B_l can include large contributions from the less varying B_r , so the pattern of field change may not be obvious. Moreover, although the contrasting behaviors of B_h in the AR core and the periphery were previously noticed in differenced vector data (Wang et al. 2009), the crucial temporal information was missing.

Our new dataset is capable of removing certain ambiguities arising from LoS only or lower-cadence vector observations. For example, Petrie & Sudol (2010) suggested that the observed step-wise B_l changes mainly result from the horizontal field changes based on the fact that the LoS flux varies more when the AR is closer to the limb. HMI 720 s vector data support the claim (Wang et al. 2012b; Petrie 2012), but lack the temporal information to reproduce the step-shaped profiles seen in the 1-minute-cadence B_l data. This can now be verified by decomposing the 135 s field vectors and comparing the more temporally resolved behaviors of B_l and B_h . The high cadence and the information returned from spectral line inversion also allow us to effectively separate magnetic imprints from transient signals. We can thus comment on the genuineness of the flare-related field changes.

Is the picture above universal? Preliminary inspection of nine ARs hosting X-class flares suggests a positive answer (Figure 6). Many other aspects of magnetic imprints beside B_h are worth exploring too. Are imprint characteristics correlated to the flare (Wang et al. 2012b) and CME properties (Sun et al. 2015)? How do the azimuth (Petrie 2013; Harker & Pevtsov 2013), electric current (Janvier et al. 2014), and magnetic topology (Zhao et al. 2014) evolve? Follow-up surveys

are straightforward and are poised to address these questions.

New advances on magnetic imprint and transient study may come from high-spectral-resolution observations or more sophisticated magnetic field inference techniques. Kleint (2017) reported step-wise changes in chromospheric B_l for an X1 flare (SOL2014-03-29T17:48) using DST/IBIS Ca II 8542 Å observations. The changes appear uncorrelated to their photospheric counterparts in HMI B_l (for ΔB_h , see Figure 6(f)). Kuckein et al. (2015) studied the photospheric and chromospheric responses in an M3 flare (SOL2013-05-17T08:57) using Si I 10827 Å and He I 10830 Å triplet observed with VTT/TIP-II. Full inversion of the Si I Stokes shows that the field strength decreases temporarily during the flare but recovers afterwards. These results illustrate a more complicated picture than that proposed above, which warrants further investigation. Upcoming NST and DKIST telescope magnetic field observations will contribute to this topic.

The origin of the magnetic imprints is not entirely clear. The coronal implosion conjecture (Hudson 2000) is often cited to explain the increase in horizontal photospheric field. We note that the model mainly concerns the contracting coronal structure; it is not guaranteed that the photosphere responds in a similar fashion. As mentioned above, even the chromospheric and photospheric field evolution seems to be dissociated (Kleint 2017). Numerical models that reproduce the implosion phenomenon may help address the issue (Zuccarello et al. 2017).

Below, we discuss a couple of implications from our results. The first point is also an attempt to explain the observation in terms of momentum conservation.

Firstly, we note that the total Lorentz force inside a volume can be expressed as a surface integral of the Maxwell stress tensor on its boundaries, fully determined by the local magnetic field (Fisher et al. 2012). If we choose a volume in the solar atmosphere that encloses the entire CME ejecta, place its lower boundary in the photosphere, and assume that the contribution from the side and top boundaries is negligible or largely invariant, the impulsive Lorentz force thought to provide the upward momentum of a CME *must* manifest as the photospheric field changes. The increases of B_h near the PIL will lead to a positive increase of the total vertical force $F_r \propto \sum (B_h^2 - B_r^2)$, which presumably drives the ejecta. It should be canceled later by a decrease of B_h in the periphery if the volume is to return to force equilibrium. In other words, the observed rapid magnetic imprint that evolves on a coronal Alfvénic time scale is a natural consequence of momentum conservation. In reality, gravitational force and thermal dynamics responses of the dense lower atmosphere complicate the situation (Sun et al. 2016). We note that this putative upward Lorentz force *inside* the volume should not be confused with the downward force exerted on the rest of the Sun by the selected volume. The latter is thought to be one possible mechanism for sunquakes (see below).

Secondly, numerical simulations of solar eruptions can be

used to verify the arguments above. We have investigated the magnetic field evolution in the lowest layers of two published MHD models (Török & Kliem 2005; Lynch et al. 2009). Preliminary analysis (Sun et al. 2016; Lynch et al. 2017) shows that both display clear magnetic imprints similar to that of AR 11158, that is, B_h increases in the AR core and decreases in the periphery, despite very different magnetic topology and eruption mechanisms. An earlier study of a third MHD model (Fan 2010) showed similar signatures (Li et al. 2011). None of these three models make assumptions that are known to produce magnetic imprints, and the agreement is unlikely a mere coincidence. We thus conjecture that the magnetic imprint may be a fundamental aspect of solar eruption.

We finally point out that the high-cadence vector magnetograms can be useful to the study of sunquakes and data-driven modeling of the solar corona, among other topics.

Sunquakes, a helioseismic response to the flare impact in the solar photosphere, have been thought to originate from high-energy electrons, protons, or radiative back-warming (e.g., Kosovichev & Zharkova 1998; Donea & Lindsey 2005; Zharkova & Zharkov 2007). Magnetic force was recently proposed as an alternative mechanism (Hudson et al. 2008; Fisher et al. 2012). The new explanation is particularly appealing for the sunquake observed in AR 11158, because the disturbance is observed before significant HXR emission, thus disfavoring a high-energy particle origin (Kosovichev 2011), and the sources appear to be co-spatial with two ends of the erupting flux rope (Figure 6(a); Zharkov et al. 2011). Nevertheless, studies of individual events have not reached a consensus (e.g., Alvarado-Gómez et al. 2012; Judge et al. 2014). To this end, a survey of sunquakes in the context of magnetic field variations will be helpful. A preliminary analysis (Chen & Zhao 2016) detects sunquake signals in five of the nine X-class flares illustrated here (Figure 6). The location, strength, and timing of the sources can now be compared with the magnetic evolution. Predictions from theoretical and numerical studies (e.g., Lindsey et al. 2014; Russell et al. 2016) regarding the role of specific magnetic configuration can also be tested.

Knowledge of the coronal magnetic field is vital to our understanding of solar eruptions and our capability to predict major space weather events. New-generation data-driven models (e.g., Cheung & DeRosa 2012; Inoue et al. 2014; Fisher et al. 2015; Galsgaard et al. 2015; Jiang et al. 2016) aim to take advantage of the observed evolution of the magnetic and velocity fields and model the evolution of the coronal field with sufficient accuracy and efficiency. Leake et al. (2017) have investigated the effect of the driving time scale, i.e., the input data cadence, on the modeling accuracy using their newly developed, data-driven MHD framework. They drive the new model with photospheric conditions sampled from a “ground-truth” flux-emergence MHD simulation (e.g., Leake et al. 2013) and compare the outcomes with the known ground-truth. Rapid evolution of the sub-AR magnetic field

cannot be recreated from a 12-minute-cadence driver. Contrarily, a 1.2-minute-cadence driver reduces the relative error in magnetic free energy by almost two orders of magnitude, down to less than 10%. The test demonstrates that the high-cadence vector data are more suited for data-driven modeling, although the higher noise can be a concern.

We thank Sébastien Couvidat, Rebecca Centeno, Monica Bobra, Jeneen Sommers, and Hao Thai for assistance with data processing. This work is supported by NASA contract NAS5-02139 (HMI), NASA awards NNX13AK39G (CGEM) and NNX14ZDA001N-HGI, and NSF SHINE award AGS1622495. The *SDO* data are courtesy of NASA and the *SDO*/HMI science team. Function fitting is performed with MPFIT (<http://purl.com/net/mpfit>).

Facility: SDO

REFERENCES

- Abramenko, V. I., & Baranovsky, E. A. 2004, *Sol. Phys.*, **220**, 81
- Alvarado-Gómez, J. D., Buitrago-Casas, J. C., Martínez-Oliveros, J. C., et al. 2012, *Sol. Phys.*, **280**, 335
- Burtseva, O., Martínez-Oliveros, J. C., Petrie, G. J. D., & Pevtsov, A. A. 2015, *ApJ*, **806**, 173
- Cameron, R., & Sammis, I. 1999, *ApJL*, **525**, L61
- Centeno, R., Schou, J., Hayashi, K., et al. 2014, *Sol. Phys.*, **289**, 3531
- Chen, R., & Zhao, J. 2016, AGU Fall Meeting Abstracts, SH43E-03
- Cheung, M. C. M., & DeRosa, M. L. 2012, *ApJ*, **757**, 147
- Cliver, E. W., Petrie, G. J. D., & Ling, A. G. 2012, *ApJ*, **756**, 144
- Donea, A.-C., & Lindsey, C. 2005, *ApJ*, **630**, 1168
- Fan, Y. 2010, *ApJ*, **719**, 728
- Fisher, G. H., Bercik, D. J., Welsch, B. T., & Hudson, H. S. 2012, *Sol. Phys.*, **277**, 59
- Fisher, G. H., ABBETT, W. P., Bercik, D. J., et al. 2015, *Space Weather*, **13**, 369
- Galsgaard, K., Madjarska, M. S., Vanninathan, K., Huang, Z., & Presmann, M. 2015, *A&A*, **584**, A39
- Gosain, S. 2012, *ApJ*, **749**, 85
- Harker, B. J., & Pevtsov, A. A. 2013, *ApJ*, **778**, 175
- Hoeksema, J. T., Liu, Y., Hayashi, K., et al. 2014, *Sol. Phys.*, **289**, 3483
- Hudson, H. S. 2000, *ApJL*, **531**, L75
- Hudson, H. S., Fisher, G. H., & Welsch, B. T. 2008, in *Astronomical Society of the Pacific Conference Series*, Vol. 383, *Subsurface and Atmospheric Influences on Solar Activity*, ed. R. Howe, R. W. Komm, K. S. Balasubramaniam, & G. J. D. Petrie, 221
- Inoue, S., Hayashi, K., Magara, T., Choe, G. S., & Park, Y. D. 2014, *ApJ*, **788**, 182
- Janvier, M., Aulanier, G., Bommier, V., et al. 2014, *ApJ*, **788**, 60
- Jiang, C., Wu, S. T., Feng, X., & Hu, Q. 2016, *Nature Communications*, **7**, 11522
- Johnstone, B. M., Petrie, G. J. D., & Sudol, J. J. 2012, *ApJ*, **760**, 29
- Judge, P. G., Kleint, L., Donea, A., Sainz Dalda, A., & Fletcher, L. 2014, *ApJ*, **796**, 85
- Kazachenko, M. D., Lynch, B. J., Welsch, B., Sun, X., & DeRosa, M. L. 2017, *ApJ*, submitted
- Kerr, G. S., & Fletcher, L. 2014, *ApJ*, **783**, 98
- Kleint, L. 2017, *ApJ*, **834**, 26
- Kosovichev, A. G. 2011, *ApJL*, **734**, L15
- Kosovichev, A. G., & Zharkova, V. V. 1998, *Nature*, **393**, 317
- . 2001, *ApJL*, **550**, L105
- Kuckein, C., Collados, M., & Manso Sainz, R. 2015, *ApJL*, **799**, L25

- Leake, J. E., Linton, M. G., & Schuck, P. W. 2017, *ApJ*, **838**, 113
- Leake, J. E., Linton, M. G., & Török, T. 2013, *ApJ*, **778**, 99
- Li, Y., Jing, J., Fan, Y., & Wang, H. 2011, *ApJL*, **727**, L19
- Lindsey, C., Donea, A.-C., Martínez Oliveros, J. C., & Hudson, H. S. 2014, *Sol. Phys.*, **289**, 1457
- Liu, C., Deng, N., Liu, Y., et al. 2005, *Appl. Phys. J.*, **622**, 722
- Liu, C., Xu, Y., Cao, W., et al. 2016a, *Nature Communications*, **7**, 13104
- Liu, Y., Baldner, C., Bogart, R. S., et al. 2016b, in AAS/Solar Physics Division Meeting, Vol. 47, AAS/Solar Physics Division Meeting, 8.10
- Lynch, B. J., Antiochos, S. K., Li, Y., Luhmann, J. G., & DeVore, C. R. 2009, *ApJ*, **697**, 1918
- Lynch, B. J., Sun, X., Török, T., & Li, Y. 2017, *ApJ*, in prep.
- Martínez Oliveros, J. C., Couvidat, S., Schou, J., et al. 2011, *Sol. Phys.*, **269**, 269
- Martínez Oliveros, J. C., Lindsey, C., Hudson, H. S., & Buitrago Casas, J. C. 2014, *Sol. Phys.*, **289**, 809
- Maurya, R. A., Vemareddy, P., & Ambastha, A. 2012, *ApJ*, **747**, 134
- Petrie, G. J. D. 2012, *ApJ*, **759**, 50
- . 2013, *Sol. Phys.*, **287**, 415
- Petrie, G. J. D., & Sudol, J. J. 2010, *ApJ*, **724**, 1218
- Qiu, J., & Gary, D. E. 2003, *ApJ*, **599**, 615
- Raja Bayanna, A., Kumar, B., Venkatakrishnan, P., et al. 2014, *Research in Astronomy and Astrophysics*, **14**, 207
- Russell, A. J. B., Mooney, M. K., Leake, J. E., & Hudson, H. S. 2016, *ApJ*, **831**, 42
- Schou, J., Scherrer, P. H., Bush, R. I., et al. 2012, *Sol. Phys.*, **275**, 229
- Schrijver, C. J. 2009, *Advances in Space Research*, **43**, 739
- Schrijver, C. J., Aulanier, G., Title, A. M., Pariat, E., & Delannée, C. 2011, *ApJ*, **738**, 167
- Sudol, J. J., & Harvey, J. W. 2005, *ApJ*, **635**, 647
- Sun, X. 2013, ArXiv e-prints, [arXiv:1309.2392](https://arxiv.org/abs/1309.2392) [astro-ph.SR]
- Sun, X., Fisher, G. H., Torok, T., et al. 2016, in AAS/Solar Physics Division Meeting, Vol. 47, AAS/Solar Physics Division Meeting, 6.28
- Sun, X., Hoeksema, J. T., Liu, Y., et al. 2012, *ApJ*, **748**, 77
- Sun, X., Bobra, M. G., Hoeksema, J. T., et al. 2015, *ApJL*, **804**, L28
- Török, T., & Kliem, B. 2005, *ApJL*, **630**, L97
- Wang, H. 1992, *Sol. Phys.*, **140**, 85
- Wang, H., Ewell, Jr., M. W., Zirin, H., & Ai, G. 1994, *ApJ*, **424**, 436
- Wang, H., & Liu, C. 2010, *ApJL*, **716**, L195
- . 2015, *Research in Astronomy and Astrophysics*, **15**, 145
- Wang, H., Spirock, T. J., Qiu, J., et al. 2002, *ApJ*, **576**, 497
- Wang, J., Zhao, M., & Zhou, G. 2009, *ApJ*, **690**, 862
- Wang, S., Liu, C., Deng, N., & Wang, H. 2014, *ApJL*, **782**, L31
- Wang, S., Liu, C., Liu, R., et al. 2012a, *ApJL*, **745**, L17
- Wang, S., Liu, C., & Wang, H. 2012b, *ApJL*, **757**, L5
- Zhao, J., Li, H., Pariat, E., et al. 2014, *ApJ*, **787**, 88
- Zharkov, S., Green, L. M., Matthews, S. A., & Zharkova, V. V. 2011, *ApJL*, **741**, L35
- Zharkova, V. V., & Zharkov, S. I. 2007, *ApJ*, **664**, 573
- Zuccarello, F. P., Aulanier, G., Dudík, J., et al. 2017, *ApJ*, **837**, 115